Constitutive signal bias mediated by the human GHRHR splice variant 1

Zhaotong Cong[a,b,1], Fulai Zhou[c,1], Chao Zhang[d,e,1] , Xinyu Zou[f,1], Huibing Zhang[g], Yuzhe Wang[e,h], Qingtong Zhou[a] , Xiaoqing Cai[c,h], Qiaofeng Liu[b], Jie Li[a], Lijun Shao[d,e], Chunyou Mao[g], Xi Wang[e,h], Jihong Wu[i], Tian Xia[f], Li-Hua Zhao[c] , Hualiang Jiang[j,k], Yan Zhang[g], H. Eric Xu[c,2], Xi Cheng[j,k,2] , Dehua Yang[c,e,h,l,2] , and Ming-Wei Wang[a,b,c,d,e,h,l,2]

[a]Department of Pharmacology, School of Basic Medical Sciences, Fudan University, Shanghai 200032, China; [b]School of Pharmacy, Fudan University, Shanghai 201203, China; [c]The CAS Key Laboratory of Receptor Research, Shanghai Institute of Materia Medica, Chinese Academy of Sciences, Shanghai 201203, China; [d]School of Life Science and Technology, ShanghaiTech University, Shanghai 201210, China; [e]University of Chinese Academy of Sciences, Beijing 100049, China; [f]School of Artificial Intelligence and Automation, Huazhong University of Science and Technology, Wuhan 430074, China; [g]Department of Biophysics, Zhejiang University School of Medicine, Hangzhou 310058, China; [h]The National Center for Drug Screening, Shanghai Institute of Materia Medica, Chinese Academy of Sciences, Shanghai 201203, China; [i]Eye and ENT Hospital, Fudan University, Shanghai 200031, China; [j]State Key Laboratory of Drug Research, Chinese Academy of Sciences, Shanghai 201203, China; [k]School of Pharmaceutical Science and Technology, Hangzhou Institute of Advanced Study, Hangzhou 310024, China; and [l]Research Center for Deep-sea Bioresources, Sanya, Hainan 572025, China

Alternative splicing of G protein–coupled receptors has been observed, but their functions are largely unknown. Here, we report that a splice variant (SV1) of the human growth hormone–releasing hormone receptor (GHRHR) is capable of transducing biased signal. Differing only at the receptor N terminus, GHRHR predominantly activates G_s while SV1 selectively couples to β-arrestins. Based on the cryogenic electron microscopy structures of SV1 in the *apo* state or GHRH-bound state in complex with the G_s protein, molecular dynamics simulations reveal that the N termini of GHRHR and SV1 differentiate the downstream signaling pathways, G_s versus β-arrestins. As suggested by mutagenesis and functional studies, it appears that GHRH-elicited signal bias toward β-arrestin recruitment is constitutively mediated by SV1. The level of SV1 expression in prostate cancer cells is also positively correlated with ERK1/2 phosphorylation but negatively correlated with cAMP response. Our findings imply that constitutive signal bias may be a mechanism that ensures cancer cell proliferation.

class B1 GPCR | receptor bias | cancer | cell proliferation

Gprotein–coupled receptors (GPCRs) are the largest superfamily of proteins in the body. They are almost expressed in every cell/tissue and transduce various signals to regulate a plethora of physiological functions (1). As a common and effective strategy to increase the functional diversity of the human genome, alternative splicing is often observed among GPCRs (2–5). The most common types of alternative splicing include exon skipping, splice site selection, and intron retention, resulting in deletion, exchange, and insertion of receptor sequences, respectively (6). Although ~50% of GPCR genes are intronless, those that possess introns have the possibility to undergo alternative splicing, thereby generating subtype isoforms that may differ in ligand binding, receptor trafficking, and signal transduction (7, 8). Some splice variants even display functional characteristics opposite to the canonical form (9).

GPCR splice variants often exhibit tissue-specific distribution and signaling characteristics that may impact disease pathology (10). For instance, Kahles et al. reported that alternative splicing events are more frequent in tumorous compared with normal tissues (11). Although splice variants of many GPCRs, such as growth hormone–releasing hormone receptor (GHRHR) (12), thromboxane receptor (13), cholecystokinin-B receptor (14), secretin receptors (15), and somatostatin receptor (16), have been detected in various cancers, their biological significance is poorly understood. While alternative splicing of the C-X-C chemokine receptor 3 (CXCR3) was linked to β-arrestin recruitment (4), expression of GHRHR splice variants could be induced by hypoxic microenvironment in solid tumors, leading enhanced glycolysis (17), suggesting that cancer-associated GPCR isoforms

are not only a consequence of cellular adaptation but also have an effect on malignancy.

We have previously revealed the structural basis of GHRHR activation and uncovered the detailed mechanism by which a naturally occurring mutation associated with isolated growth hormone deficiency leads to impaired GHRHR function (18). While the primary role of GHRHR is to stimulate growth hormone synthesis and secretion from the anterior pituitary somatotrophs upon GHRH binding (19), its ectopic expression in cancers has been studied extensively (20, 21). Both GHRH and GHRHR are present in lung (22), mammary (23), ovarian (24), endometrial (25), gastric (26), colorectal (27), ocular (28), prostatic (29, 30), and pancreatic (27) cancers. The cancer cell growth could be stimulated by exogenous GHRH and, conversely, inhibited by GHRHR antagonists (31). Among the four splice variants (SVs), SV1 possesses the greatest similarity to the full-length GHRHR and remains functional by eliciting cAMP signaling and mitogenic activity upon GHRH stimulation (32, 33). Due to its physical presence and bioactivity in cancer progression, SV1 is also called tumoral GHRHR that coexists with pituitary GHRHR in most tumors. Compared with GHRHR, SV1 lacks a portion of the

Significance

The mechanism of functional changes induced by alternative splicing of GHRHR is largely unknown. Here, we demonstrate that GHRH-elicited signal bias toward β-arrestin recruitment is constitutively mediated by SV1. The cryogenic electron microscopy structures of SV1 and molecular dynamics simulations reveal the different functionalities between GHRHR and SV1 at the near-atomic level (i.e., the N termini of GHRHR and SV1 differentiate the downstream signaling pathways, G_s versus β-arrestins). Our findings provide valuable insights into the functional diversity of class B1 GPCRs that may aid in the design of better therapeutic agents against certain cancers.

extracellular domain (ECD) because the first three exons are replaced by a fragment of intron 3, leading to the replacement of the first 89 amino acids of GHRHR with a distinct 25-amino acid sequence (12). Through functional diversity evaluation of almost all reported GPCR isoforms, Marti-Solano et al. found that the N-terminal splicing is the most frequently occurring structural variation and tends to alter ligand binding and/or signal transduction (34). In the case of SV1, changes of ligand-binding affinities (35) and signaling properties are connected with its mitogenic effect (33, 36–40), but the underlying mechanism has yet to be elucidated.

Here, we report the cryogenic electron microscopy (cryo-EM) structures of both the *apo* state and GHRH-bound SV1 in complex with G_s protein. Together with previously published GHRH–GHRHR–G_s complex structure (18), we are able to show the molecular details of ligand recognition and SV1 activation. In-depth investigations on SV1-mediated signal transduction unveiled a constitutively biased signaling pathway, thereby offering new insights into the role of alternative splicing of a class B1 GPCR in cancer cell proliferation.

Results

SV1 Inhibits G_s Activation. To better understand the functional outcome of alternative splicing of GHRHR, we evaluated the ability of SV1 to activate G_s upon stimulation by GHRH in the human embryonic kidney 293tsA1609neo (HEK293T) cells. Hemagglutinin (HA) signal peptide was fused to the Flag-tagged N terminus to rescue the cell surface expression level of SV1, which remained stable across all assays. G_s activation was assessed using split luciferase NanoBiT G protein sensors to determine GHRH-induced decreases in luminescence on a time-course. For SV1, the G_s sensor gave a similar decrease in luminescence to GHRHR, suggesting that both caused the same G_s conformational change. However, GHRH concentration-response curves showed that the ability of SV1 to activate G_s was significantly impaired (Fig. 1A), as E_{max} and EC_{50} values were reduced (*SI Appendix*, Table S1). G_s-mediated cAMP accumulation was also drastically decreased (by almost 1,000-fold) in cells expressing SV1 compared with that of GHRHR (Fig. 1B and *SI Appendix*, Table S2). As expected, removal of the N-terminal 89 residues in GHRHR to imitate SV1 or deletion of the entire ECD led to diminished cAMP responses. In conjunction with the consequences
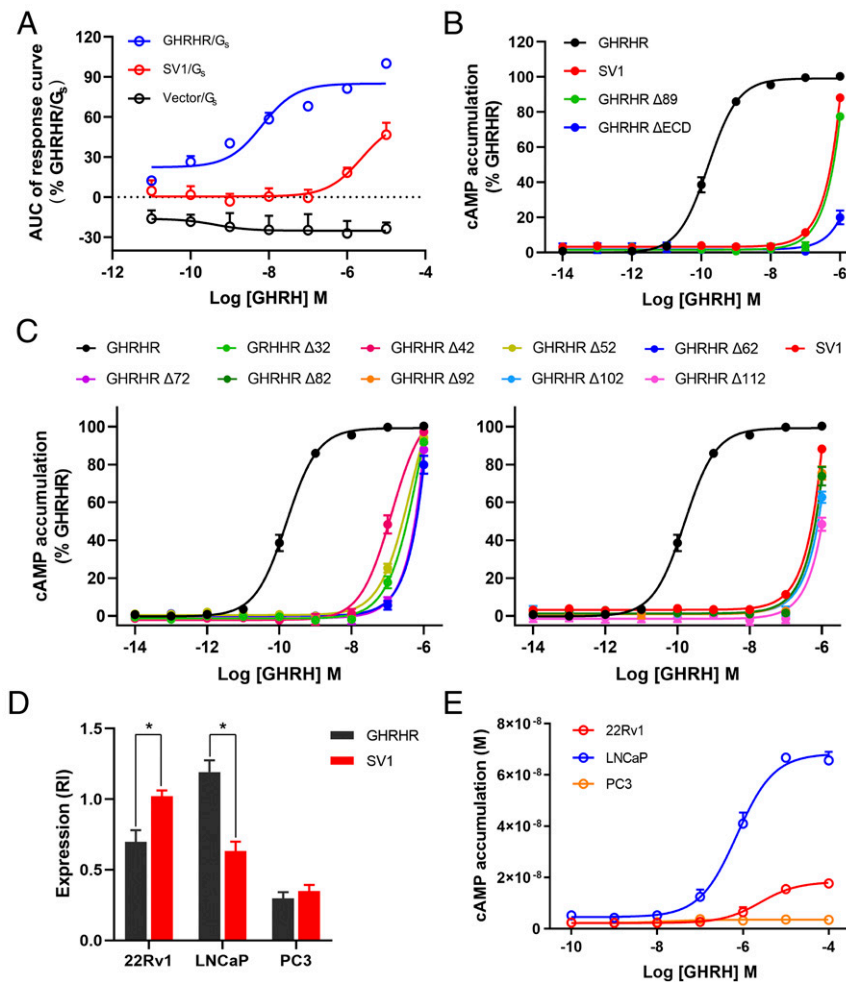
Fig. 1. GHRH-induced G_s protein coupling and cAMP signaling mediated by GHRHR and SV1. (A) GHRH-induced conformational changes in the trimeric G_s protein. Concentration-response curves are expressed as AUC across the time-course response curve (0 to 25 min) for each concentration and normalized to GHRHR. (B and C) Concentration-response curves of cAMP accumulation at GHRHR and SV1. Comparison of SV1 with full-length or truncated GHRHR that lacks ECD or the first 89 residues (B). Comparison of SV1 with various N terminus truncated GHRHRs (C). (D) Expression of GHRHR and SV1 in prostate cancer cell lines. Protein levels were estimated as relative intensity (RI) compared with β-tubulin (loading control). (E) Concentration-response curves of cAMP accumulation in prostate cancer cells. Data shown are means ± SEM of at least three independent experiments (n = 3 to 5) performed in quadruplicate. Δ, truncation; *P < 0.05; **P < 0.01.

of sequential deletion of 10 residues in the ECD of GHRHR, our results point to the importance of the N terminus in maintaining GHRHR function (Fig. 1C). GHRH-induced cAMP responses were subsequently measured in three prostate cancer cell lines expressing different levels of GHRHR and SV1. In line with previous findings (29, 30), LNCaP and 22Rv1 cells expressed high levels of GHRHR and SV1, respectively, while PC3 cells had low expression levels of both (Fig. 1D and *SI Appendix*, Fig. S1C). It was found that LNCaP cells displayed the strongest cAMP response, whereas 22Rv1 and PC3 cells exhibited either markedly reduced or marginal cAMP responses (Fig. 1E).

SV1 Enhances β-arrestin Recruitment. Since SV1 promotes cell proliferation and β-arrestin per se has protumorigenic properties (41, 42), it is possible that SV1 may potentially behave as a β-arrestin–biased variant that facilitates cancer cell growth. To test this hypothesis, we measured GHRH-induced β-arrestin recruitment and observed that SV1 indeed increased both β-arrestin 1 and β-arrestin 2 recruitment by about 10% and 25% at 0.25 mM GHRH, respectively, compared with that of GHRHR (Fig. 2A). β-arrestin 1/2 recruitments were also enhanced following truncation of the first 89 residues or the entire ECD; it was not affected if the deletion was made before the first 82 residues (Fig. 2B), suggesting that this biased signaling is caused by a structural change in the ECD of GHRHR. We next measured ERK1/2

phosphorylation (pERK1/2) upon GHRH stimulation in HEK293T cells expressing GHRHR or SV1. In cells expressing SV1, GHRH induced a stronger pERK1/2 response, which was about 40% higher than that of GHRHR at the peak response time (Fig. 2C and *SI Appendix*, Fig. S1A). To examine if the ERK phosphorylation was GHRHR- or SV1-dependent, the cells were also treated with a GHRHR antagonist, MIA-602, before GHRH stimulation. Inhibition of pERK1/2 by MIA-602 indicates that GHRH could specifically activate this signaling pathway (Fig. 2C and *SI Appendix*, Fig. S1A). Consistent with previous findings showing that SV1 promotes cell proliferation via pERK1/2 pathway (30, 40), we found that SV1 expression is correlated with the cell cycle. One micromolar of GHRH augmented the number of cells in G_2/M phase (increased from 22.8 to 37.7%) but diminished that corresponding to G_1 phase (decreased from 46.6 to 32.8%) (*SI Appendix*, Fig. S1C). Among the three prostate cancer cell lines, only 22Rv1 that expresses a high level of SV1 displayed a markedly stronger and longer pERK1/2 response that could be inhibited by MIA-602 (Fig. 2D and *SI Appendix*, Fig. S1B).

Structure Comparison between GHRHR and SV1. To obtain a stable SV1 complex for the cryo-EM study, we removed 18 amino acids at the C terminus and employed the NanoBiT tethering strategy (18, 43) to further stabilize the assembly of SV1 with G_s heterotrimer (*SI Appendix*, Fig. S2). The structures of GHRH–SV1–G_s
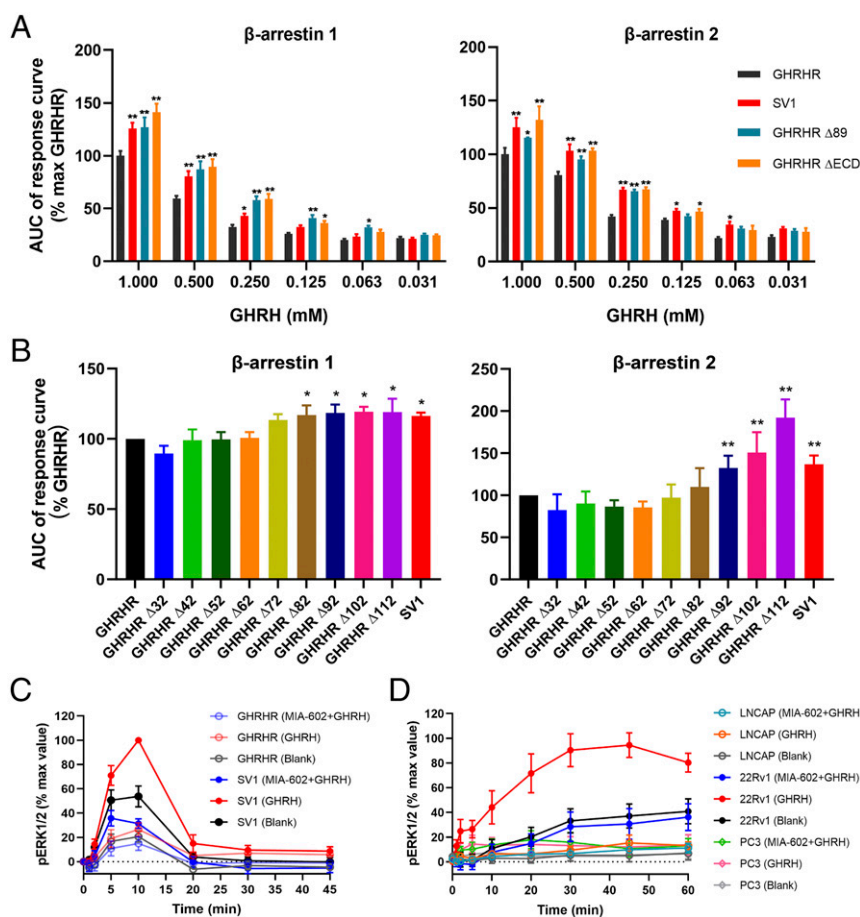
Fig. 2. GHRH-induced β-arrestin recruitment and pERK1/2 signaling mediated by GHRHR and SV1. (A and B) β-arrestin recruitment by GHRHR and SV1. Comparison of SV1 with full-length or truncated GHRHR that lacks the entire ECD or the first 89 residues (A). Comparison of SV1 and various N terminus truncated GHRHRs. The assay was initiated by 250 μM GHRH (B). The response was calculated as AUC across the full kinetic trace. *P < 0.01 and **P < 0.001 compared with GHRHR; Δ, truncation. (C and D) Time-course of ERK1/2 activation. The assay was initiated by 1 μM GHRH and inhibition was achieved by 4 μM MIA-602 in HEK293T cells expressing GHRHR or SV1 (C) and prostate cancer cell lines (D). Data shown are means ± SEM of at least four independent experiments (n = 4 to 6) performed in duplicate. *P < 0.05; **P < 0.01.

Cong et al.
Constitutive signal bias mediated by the human GHRHR splice variant 1

PNAS | 3 of 10
https://doi.org/10.1073/pnas.2106606118

and SV1–G$_s$ (*apo*) complexes were determined by single-particle cryo-EM at global resolutions of 3.3 and 2.6 Å, respectively (Fig. 3 and *SI Appendix*, Figs. S3 and S4C and Table S3). The high-quality density maps allowed unambiguous building for receptor residues L55$^{1.29b}$ to H328$^{8.59b}$ [class B GPCR numbering in superscript (44)], GHRH (residues Y1^P-A19^P), and most residues of nanobody 35 (Nb35) and Gαβγ subunits except the α-helical domain (AHD) of Gα$_s$. The majority of amino acid side chains, except for residues C131^{ECL1}-S132^{ECL1} as well as P249^{ICL3}-H255$^{6.30b}$ in the *apo* SV1–G$_s$ complex and residues P249^{ICL3}-Q255$^{6.32b}$ in the GHRH–SV1–G$_s$ complex, were well resolved in the final models (*SI Appendix*, Fig. S5).
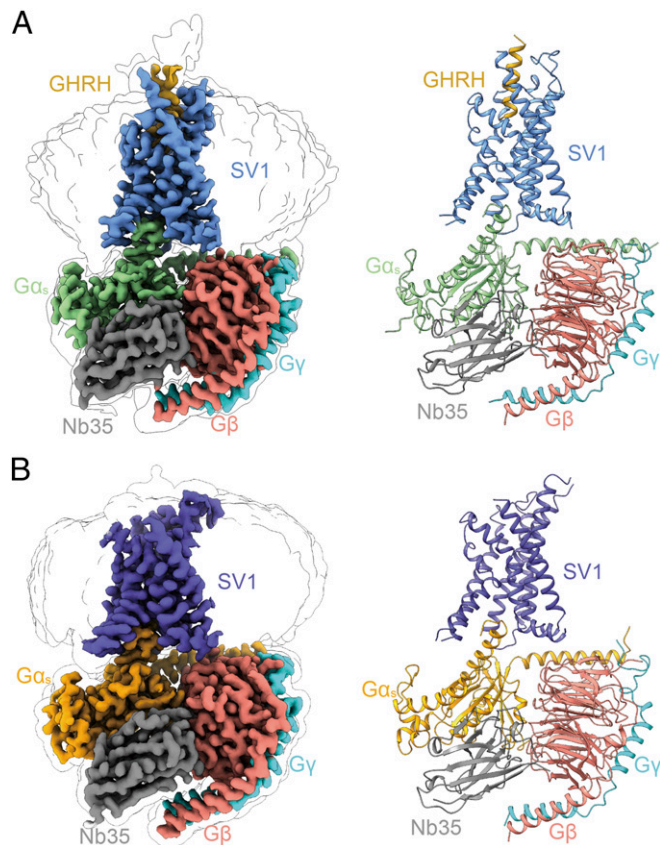
In the GHRH–SV1–G$_s$ complex structure, the bundle of seven transmembrane helices adopts highly similar conformations to that of the GHRH–GHRHR–G$_s$ complex (18) with a Cα root-mean-square deviation of 0.5 Å (Fig. 4A). This was expected, considering that the amino acid sequences of transmembrane domain (TMD) are identical between SV1 and GHRHR. However, the interactions between ECD and GHRH are remarkably different in the two complexes. In the GHRH–SV1–G$_s$ complex, its ECD does not stabilize the binding by GHRH (Fig. 4A), while that of GHRHR has rich interactions with GHRH involving residues L34^{ECD}, L62^{ECD}, F82^{ECD}, and F85^{ECD} (Fig. 4B). Substituting any or all of these four ECD residues with alanine reduced GHRHR-elicited cAMP responses (*SI Appendix*, Fig. S6B and Table S2) but enhanced β-arrestin 1/2 recruitments (*SI Appendix*,

Fig. 3. Overall structures of GHRH–SV1–Gα$_s$ and *apo* SV1–Gα$_s$ complexes. (A) Orthogonal views of the density map (*Left*) and the model (*Right*) for the GHRH–SV1–Gα$_s$–Nb35 complex. SV1, GHRH, Gα$_s$, Gβ, Gγ, and Nb35 are colored cornflower blue, gold, light green, salmon, cyan, and gray, respectively. (B) Orthogonal views of the density map (*Left*) and the model (*Right*) for the *apo* SV1–Gα$_s$–Nb35 complex. SV1, Gα$_s$, Gβ, Gγ, and Nb35 are colored slate blue, orange, salmon, cyan, and gray, respectively. The structures are shown in cartoon representation.

Fig. S6A), similar to SV1. These findings underscored the importance of the N-terminal ECD residues in determining signal bias upon GHRH stimulation. Notably, without stable interactions with residues in the SV1 ECD, the C terminus of GHRH is highly flexible. Consequently, the resolvable region of GHRH in the GHRH–SV1–G$_s$ complex is 10 residues shorter at the C terminus than that in the GHRH–GHRHR–G$_s$ complex (Fig. 4A). In the GHRHR complex structure, GHRH has a slightly larger tilting angle than that in the SV1 complex structure due to its interactions with the ECD of GHRHR (*SI Appendix*, Fig. S7). Nevertheless, due to resembling TMD conformations, the N terminus of GHRH binds to the orthosteric pocket of SV1 with an orientation similar to that in the GHRH–GHRHR–G$_s$ complex (Fig. 4A).
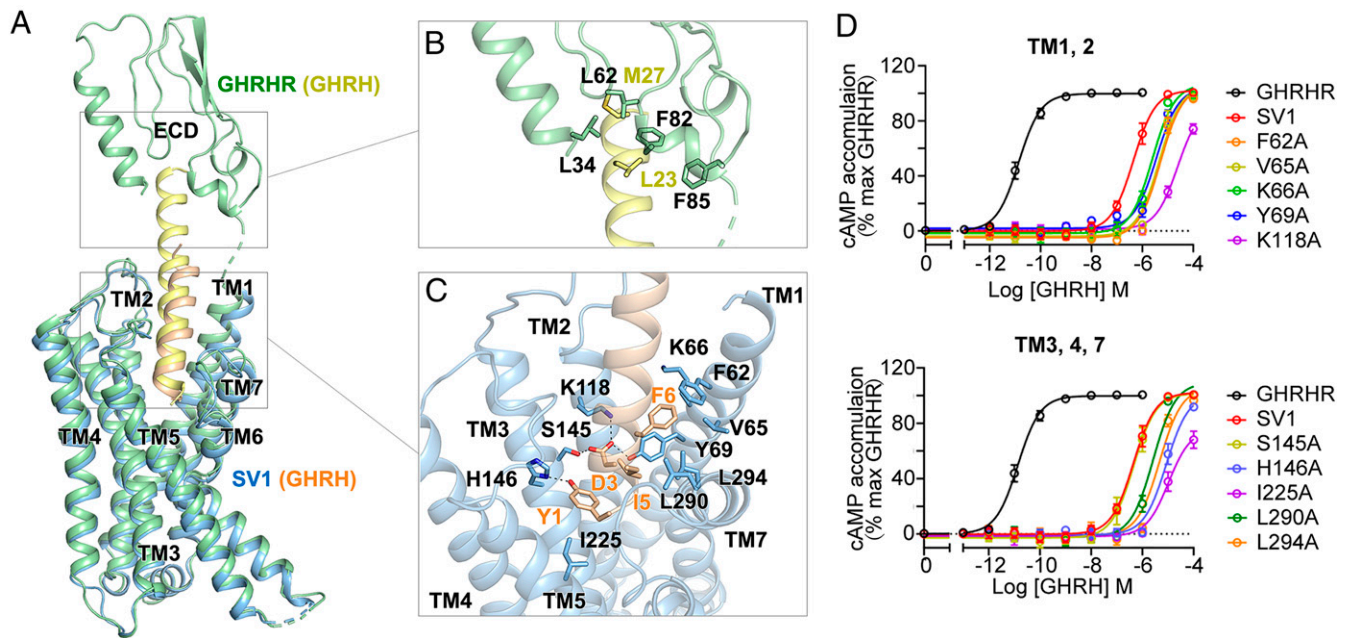
The GHRH–SV1–G$_s$ complex structure shows that GHRH binds to SV1 through a continuous interacting network involving TMD helices (TMs 1 to 4 and TM7) (Fig. 4 A and C). The N terminus of GHRH deeply inserts into the receptor core. Y1^P of GHRH forms hydrogen bonds with H146$^{3.37b}$ and hydrophobic interactions with I225$^{5.43b}$. D3^P makes salt bridges with K118$^{2.67b}$, which is further strengthened by hydrogen bonding with Y69$^{1.43b}$ and S145$^{3.36b}$. I5^P has van der Waals interactions with two TM7 residues, i.e., L290$^{7.35b}$ and L294$^{7.39b}$. F6^P builds extensive hydrophobic contacts with F62$^{1.36b}$, V65$^{1.39b}$, and K66$^{1.40b}$. Impairing these contacts dramatically decreased the potency of GHRH-induced cAMP accumulation mediated by SV1 (Fig. 4D and *SI Appendix*, Table S4), suggesting essential roles of these residues in ligand recognition and receptor activation. Meanwhile, binding of GHRH yields to an extended helical conformation of TM1 and inward movements of ECLs 1 and 2 to the peptide-binding pocket of SV1 (*SI Appendix*, Fig. S8).

Interaction between SV1 and β-arrestin 1. To gain insights into the molecular mechanism by which β-arrestins bind to GHRHR and SV1, we performed molecular dynamics (MD) simulations of arrestin-bound receptors. Because previous structural studies have reported a few β-arrestin 1–bound GPCR complexes but there is none complexed with β-arrestin 2, we constructed two simulation systems for GHRHR and SV1 bound to β-arrestin 1, respectively. In the GHRHR simulations, the ECD constantly bound to GHRH (Fig. 5 A and B and *SI Appendix*, Fig. S9A). Multiple hydrophobic ECD residues (F30^{ECD}, I31^{ECD}, L34^{ECD}, L62^{ECD}, F81^{ECD}, F82^{ECD}, and F85^{ECD}) of GHRHR frequently interacted with GHRH to stabilize its binding during simulations (Fig. 5C and *SI Appendix*, Fig. S9A). On the contrary, in the SV1 system, the short ECD of the receptor did not stably interact with the peptide (Fig. 5 A and B), resulting in an outward movement of GHRH at the extracellular side (Fig. 5B). The average minimal distance between GHRH and the bottom of the peptide-binding pocket of SV1 was 6.5 ± 1.6 Å, ~3 Å longer than that of the GHRHR system (3.4 ± 0.2 Å). In the GHRHR simulations, GHRH stably bound to the peptide-binding pocket and frequently interacted with ECL2 (Fig. 5D). Notably, the peptide residue R11^P could form a salt bridge with D274^{ECL2} in the GHRHR system. These observations suggest that the ECD of GHRHR binds to GHRH to stabilize its orientation in the peptide-binding pocket and further enhances its interactions with ECL2 at the extracellular interface. However, the ECD of SV1 is too short to stabilize the orientation of GHRH that failed to interact with ECL2 (Fig. 5D).

As a loop-linking TM5 helix, ECL2 contributes to determining its orientation. Interacting with GHRH, the ECL2 of GHRHR stayed adjacent to the peptide-binding pocket and pulled TM5 helix toward the pocket center, which contributed to a compact bundle of helices TM3, TM5, and TM6 (Fig. 5D). In particular, TM5 residue N296$^{5.50b}$ formed a hydrogen bond with the backbone oxygen of TM6 residue F338$^{6.49b}$, and TM6 residue L337$^{6.48b}$ stably interacted with the hydrophobic part of TM3 residue E223$^{3.50b}$ at the receptor core of GHRHR (Fig. 5E). In the SV1

Fig. 4. Structural comparison between SV1 and GHRHR. (*A*) Comparison between the cryo-EM structures of GHRH–SV1–G_s and GHRH–GHRHR–G_s complexes. Receptors and GHRH are shown in cartoon: GHRHR is colored in green, SV1 in blue, and GHRH in wheat and yellow. G_s is omitted for clarity. (*B*) Detailed interaction between GHRH (yellow) and the ECD of GHRHR (green). Key residues are shown as sticks. (*C*) Detailed interaction between GHRH (wheat) and the peptide-binding pocket of SV1 (blue). Salt bridges and hydrogen bonds are shown as dashed lines. (*D*) Effects of mutations in the peptide-binding pocket of SV1 on cAMP accumulation. Data shown are means ± SEM of four independent experiments (*n* = 4) conducted in quadruplicate.
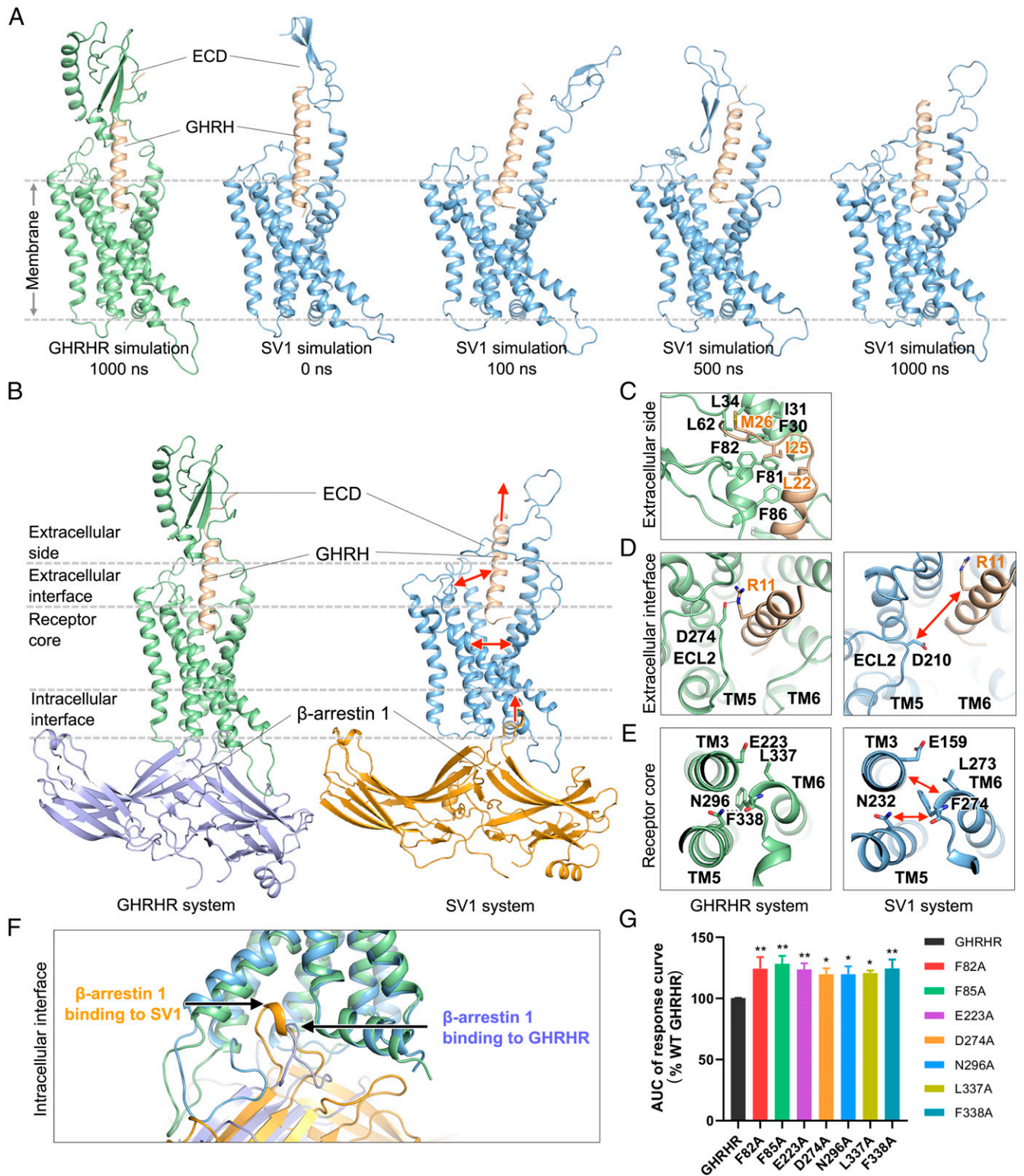
simulations, ECL2 did not stably interact with GHRH and wandered around the extracellular interface, thereby disrupting the interactions among helices TM3, TM5, and TM6 (Fig. 5*E*). The average minimal backbone distance between TM3 and TM6 increased to 7.3 ± 0.7 Å, and the backbone distance between TM5 and TM6 increased to 7.1 ± 0.5 Å. No hydrogen bonding was formed between TM5 and TM6 at the receptor core during the SV1 simulations (Fig. 5*E*). The hydrophobic interaction between the TM3 glutamic acid (E159$^{3.50b}$) and the TM6 leucine (L273$^{6.48b}$) of SV1 was also missing (Fig. 5*E*). As the interhelical distances among TM3, TM5, and TM6 increased, the volume of arrestin-binding pocket of SV1 enlarged to 2,441.3 ± 99.1 Å^3 at the intracellular side, ~300 Å^3 larger than that of GHRHR (*SI Appendix*, Fig. S9*B*). Consequentially, β-arrestin 1 had a deeper insertion toward the receptor core of SV1 (Fig. 5*F*). Compared with the GHRHR system, the insertion of β-arrestin 1 into SV1 was ~3 Å deeper along the axis perpendicular to the membrane (*z* axis in a simulation system). During the SV1 simulations, the finger loop of β-arrestin 1 exhibited more interactions with the receptor. Particularly, L68 of β-arrestin 1 stably interacted with the TM3 residues L163$^{3.54b}$ and L166$^{3.57b}$ of SV1, but did not interact with TM3 of GHRHR (*SI Appendix*, Fig. S9*C*). These findings indicate that SV1 might provide a more favorable binding interface for β-arrestin 1 compared with GHRHR. Collectively, with a short ECD, SV1 might be unable to stabilize the orientation of GHRH and therefore could not maintain the interaction between GHRH and ECL2, leading to a loop bundle of helices TM3, TM5, and TM6 and an enlarged favorable arrestin-binding pocket. For GHRHR, the full-length ECD stabilizes GHRH and facilitates GHRH binding to ECL2, which might make a compact bundle of helices TM3, TM5, and TM6 and a less favorable pocket for arrestin binding. To validate this hypothesis, we designed single-point mutations in the crucial domain of GHRHR mentioned previously. Substituting a residue in these domains (F82^{ECD} and F85^{ECD} in ECD, D274^{ECL2} in ECL2, E223$^{3.50b}$ in TM3, N296$^{5.50b}$ in TM5, and L337$^{6.48b}$ and F338$^{6.49b}$ in TM6) with alanine

significantly increased the capability of GHRHR to recruit β-arrestin 1 (Fig. 5*G* and *SI Appendix*, Fig. S6*C*), fully supporting our hypothesis.

Discussion

Although both GHRHR and SV1 are present in prostatic (45), breast (46), gastric (27), ovarian (47), pancreatic (37), lung (48), esophageal (17), oral (38, 49), and skin cancers (50), SV1 possess stronger mitogenic activities (36, 39, 40). A recent study demonstrates that alternative splicing of GHRHR, promoted by hypoxic microenvironment in solid tumors, is actually a cellular adaptation mechanism that induces cancer cell proliferation and migration (17). As a splice variant of GHRHR, SV1 only differs by 89 amino acids at its N terminus but causes a distinct biased signaling that may involve a complex regulatory mechanism associated with cancer development.

Integrating structure determination with functional studies, we reveal that splicing-encoded structural difference in the ECD of GHRHR can alter its signaling preference. Compared with GHRHR, which predominantly couples to G_s, SV1 preferentially activates β-arrestins. Removal of the N-terminal 89 residues in GHRHR to imitate the splicing or deletion of the entire ECD led to diminished cAMP responses and enhanced β-arrestin 1/2 recruitments, pointing to the importance of the N terminus in the constitutive signal bias. To uncover the molecular basis of this phenomenon, we solved the cryo-EM structures of SV1 in the *apo* state and GHRH-bound state in complex with G_s protein. In addition, we performed MD simulations to study conformational changes of SV1 mediated by β-arrestin 1 that may subsequently differentiate the downstream signaling pathways. The positive correlation of pERK1/2 and the negative correlation of cAMP accumulations with SV1 expression levels in prostate cancer cells imply a linkage with cancer. Therefore, modification of GHRHR by splicing at the N terminus results in biased arrestin signaling that might be advantageous to tumor cells.

Cong et al.
Constitutive signal bias mediated by the human GHRHR splice variant 1

PNAS | 5 of 10
https://doi.org/10.1073/pnas.2106606118

Fig. 5. β-arrestin 1 binding to GHRHR and SV1. (*A*) Distinct ECD conformations of GHRHR and SV1 during simulations. Receptors and GHRH are shown in cartoon: GHRHR is colored in green, SV1 in blue, and GHRH in wheat. β-arrestin 1 is omitted for clarity. (*B*) Representative simulation snapshots from GHRHR (*Left*) and SV1 (*Right*) systems. Gray dashed lines split the different regions of a receptor. (*C*) A representative simulation snapshot showing key interactions between GHRH (wheat) and the ECD of GHRHR (green). Key residues are shown as sticks. (*D*) Representative simulation snapshots showing the extracellular interfaces of GHRHR (*Left*) and SV1 (*Right*). A salt bridge of GHRHR (green) is shown as a black dashed line. (*E*) Representative simulation snapshots showing the receptor cores of GHRHR (*Left*) and SV1 (*Right*). A hydrogen bond of GHRH (green) is shown as a black dashed line. (*F*) Binding of β-arrestin 1 to GHRHR (green) and SV1 (blue) at the intracellular side in simulations. (*G*) β-arrestin 1 recruitment by GHRHR and its mutants. The assay was stimulated by 250 μM GHRH. Data shown are means ± SEM of at least three independent experiments (*n* = 3 to 6) performed in duplicate; *P < 0.05, **P < 0.01.

Constitutive signal bias mediated by the human GHRHR splice variant 1

Based on the SV1 structural information, MD simulations, and mutagenesis analysis, we found that alternation of the ECD might change the intracellular interface that binds to β-arrestins. In the case of GHRHR, its full-length ECD stably constrains the orientation of GHRH and facilitates the interaction between ECL2 and GHRH, which might lead to a compact bundle of TMD and a less favorable intracellular interface for β-arrestins. In contrast, with a shorter and flexible ECD, SV1 does not stabilize the interaction between GHRH and ECL2 but possibly contributes to a loop bundle of helices TM3, TM5, and TM6 and a binding pocket permitting optimal insertion of the finger loop of β-arrestins. The ECD residues efficiently regulate signal bias via interacting with ligand. Particularly, four hydrophobic residues of GHRHR ($L34^{ECD}$, $L62^{ECD}$, $F82^{ECD}$, and $F85^{ECD}$) bound to GHRH are identified as key ECD elements that determine the nature of downstream signals. Substituting them with alanine significantly decreased cAMP responses (*SI Appendix*, Fig. S6*B*). F82A and F85A mutants of GHRHR enhanced β-arrestin 1/2 recruitments, similar to that seen with SV1 (*SI Appendix*, Fig. S6*A*) and consistent with the outcome of ECD truncation (Figs. 1 and 2).

Alternation of N termini has been reported to modulate ligand binding and/or activity of a number of GPCRs (34). For instance, the N-terminal residues of CXCR3 determine its selectivity to a particular effector, i.e., β-arrestin 2 (4). In addition to ECD, ECL2 may also play an essential role in transducing signal from the extracellular side to the receptor core. Substitution of $D274^{ECL2}$ with an alanine enhances β-arrestin signaling (Fig. 5*G*). The interaction between ECL2 and parathyroid hormone (PTH) facilitates β-arrestin recruitments by PTH receptor type 1 (51). In the receptor core, TMD helices rearrange in favor of interacting with G protein or β-arrestins. Disruption of the TMD helices rearrangement by substituting $E223^{3.50b}$, $N296^{5.50b}$, $L337^{6.48b}$, and $F338^{6.49b}$ in GHRHR with alanine caused a biased β-arrestin signaling (Fig. 5*G*). The proposed molecular mechanism unveils the potential roles of ECD, ECL2, and TMD in signal bias, which might extend to other class B1 GPCRs.

The signal bias of GPCRs can be classified as ligand bias and receptor bias (52). As a principal component to initiate signaling, a receptor itself is capable of constitutively biasing downstream signal transduction through genetic variations, including a splice variant. A number of naturally occurring mutations were found to alter signaling pathways of GPCRs (52). For example, substitution of a TM6 residue of α1-adrenergic receptor led to constitutive G protein activity (53); a leucine-to-glutamine mutation in the TM3 helix of cysteinyl-leukotriene receptor 2 strongly drove $G_{q/11}$ signaling (54); and mutations in the C terminus of several class A GPCRs, including apelin receptor and neuropeptide Y4 receptor, diminished β-arrestin recruitments (55, 56). Although many genetic variations of GPCRs have been detected (34), the mechanisms governing signal bias are poorly understood. In this work, we show that a splice variant strongly drives β-arrestin recruitment by averting the canonical signaling, which is biased to G_s pathway. This structural alternation not only allows normal cells to function via a full-length receptor but also permits cancer cells to proliferate through a splice variant upon stimulation by the same endogenous ligand. Our findings thus provide insights into functional diversity of class B1 GPCRs and offer valuable information to the design of better therapeutics against certain cancers.

Materials and Methods

Cell Culture. *Spodoptera frugiperda* (*Sf*9) insect cells (Expression Systems) were grown in ESF 921 serum-free medium (Expression Systems) at 27 °C and 120 rpm. HEK293T cells were purchased from American Type Culture Collection (ATCC), cultured in Dulbecco's modified Eagle's medium (DMEM; Life Technologies), supplemented with 10% fetal bovine serum (FBS; Gibco), and maintained in a humidified chamber with 5% CO_2 at 37 °C. The PC3 prostate cancer cell line (ATCC) was cultured in F12 medium supplemented with 10% FBS and maintained in a humidified chamber with 5% CO_2 at 37 °C. 22Rv1

and LNCaP human prostate cancer cells (ATCC) were cultured in Roswell Park Memorial Institute (RPMI)-1640 medium supplemented with 10% FBS and maintained in a humidified atmosphere containing 5% CO_2 at 37 °C.

Constructs of SV1 and G_s Heterotrimer. To facilitate the expression and purification, human wild-type (WT) SV1 gene with the hemagglutinin (HA) signal peptide at its N terminus, 18 amino acids (A342-C359) truncation, and a TEV protease cleavage site followed by a double maltose-binding protein tag at its C terminus were cloned into the pFastBac vector (Invitrogen). To obtain an SV1–G_s complex with good homogeneity and stability, we used the NanoBiT tethering strategy (18, 43, 57), in which the C terminus of rat Gβ1 was linked to HiBiT subunit and the C terminus of SV1 was directly attached to LgBiT subunit with a 15-amino acid polypeptide (GSSGGGGSGGGGSSG) linker. A dominant-negative human Gα$_s$ (DNGα$_s$) was generated by site-directed mutagenesis as previously described (58) to limit G protein dissociation. An engineered G_s construct (G112) was designed based on mini-G_s (59, 60) that was employed in the determination of $A_{2A}R$-mini-G_s crystal structure (61). It was used to purify the *apo* state SV1–G_s complex. By replacing N-terminal histidine tag (His6) and TEV protease cleavage site with the N-terminal 18 amino acids (M1 to M18) of human G_{i1}, the chimeric G_s was capable of binding to scFv16, which was used to stabilize the GPCR-G_i or GPCR-G_{11} complexes (62, 63). Additionally, replacement of the GGSGGSGG linker at position of original Gα$_s$ AHD (V65-L203) with that of human G_{i1} (G60-K180) provided the binding site for Fab_G50, an antibody fragment that was used to stabilize the rhodopsin-G_i complex (64). Furthermore, three mutations (G226A, L272D, and A366S) were also incorporated by site-directed mutagenesis as previously described to further increase the dominant-negative effect by stabilizing the Gαβγ heterotrimer (59). These modifications enabled the application of different nanobodies or antibody fragments to stabilize the receptor-G_s complex, although Nb35 was solely used during SV1–G_s complex formation and stabilization in this study. The engineered G_s has also been employed and validated in the cryo-EM structure determination of the vasopressin V2 receptor–G protein complex (59).

Expression and Purification of Nanobody 35. Nb35 with a C-terminal histidine tag (His6) was expressed in *Escherichia coli* BL21 (DE3) bacteria and cultured in Terrific Broth medium supplemented with 2 mM $MgCl_2$, 0.1% (wt/vol) glucose, and 50 µg/mL ampicillin to an OD_{600} value of 1.0 at 37 °C. The cultures were then induced by 1 mM isopropyl-β-d-thiogalactoside and grown for 5 h at 37 °C. Cells were harvested by centrifugation (4,000 rpm, 20 min), and Nb35 protein was extracted and purified by nickel affinity chromatography as previously described (65). Eluted protein was concentrated and subjected to a HiLoad 16/600 Superdex 75 column (GE Healthcare) pre-equilibrated with buffer containing 20 mM 4-(2-hydroxyethyl)-1-piperazineethanesulfonic acid (HEPES), pH 7.5, and 100 mM NaCl. The monomeric fractions supplemented with 30% (vol/vol) glycerol were flash frozen in liquid nitrogen and stored in −80 °C until use.

Expression and Purification of the SV1-G_s Complex. *Sf*9 insect cells were cultured at a density of 3×10^6 cells per milliliter and coinfected with SV1-15AA-LgBiT, DNGα$_s$ or engineered G_s, Gβ1-15AA-peptide 86, and Gγ2 baculoviruses at a 1:1:1:1 ratio. The cells were then harvested by centrifugation 48 h postinfection and stored at −80 °C for future use. The frozen cells were thawed on ice and resuspended in lysis buffer containing 20 mM HEPES, pH 7.5, 100 mM NaCl, 10% (vol/vol) glycerol, 10 mM $MgCl_2$, 5 mM $CaCl_2$, 1 mM $MnCl_2$, and 100 µM Tris(2-carboxyethyl)phosphine (TCEP; Sigma-Aldrich) and supplemented with ethylene diamine tetraacetic acid (EDTA)–free protease inhibitor mixture (Bimake). Cells were lysed by dounce homogenization, and complex formation was initiated in the presence of 10 µg/mL Nb35, 25 mU/mL apyrase (Sigma-Aldrich) and 20 µM GHRH (GL Biochem) for 1.5 h at room temperature (RT). The membrane was then solubilized by adding 0.5% (wt/vol) lauryl maltose neopentyl glycol (LMNG; Anatrace) and 0.1% (wt/vol) cholesterol hemisuccinate (CHS; Anatrace) for 2 h at 4 °C. After centrifugation at 30,000 rpm for 30 min, the sample was clarified, and the supernatant was incubated with amylose resin (New England Biolabs) for 3 h at 4 °C. After incubation, the resin was collected by centrifugation (600 × *g*, 10 min) and loaded to a gravity flow column, followed by five column volumes wash of buffer A containing 20 mM HEPES, pH 7.5, 100 mM NaCl, 10% (vol/vol) glycerol, 5 mM $MgCl_2$, 1 mM $MnCl_2$, 2 µM GHRH, 25 µM TCEP, 0.1% (wt/vol) LMNG, and 0.02% (wt/vol) CHS and 15 column volumes wash of buffer B containing 20 mM HEPES, pH 7.5, 100 mM NaCl, 10% (vol/vol) glycerol, 5 mM $MgCl_2$, 1 mM $MnCl_2$, 2 µM GHRH, 25 µM TCEP, 0.03% (wt/vol) LMNG, 0.01% (wt/vol) glyco-diosgenin (Anatrace), and 0.008% (wt/vol) CHS. The bound samples were incubated with His-tagged TEV protease (customer-made) overnight at 4 °C in buffer B. The flow

Cong et al.
Constitutive signal bias mediated by the human GHRHR splice variant 1

PNAS | 7 of 10
https://doi.org/10.1073/pnas.2106606118

through was collected next day, concentrated using an Amicon Ultra centrifugal filter (molecular weight cutoff at 100 kDa, Millipore) and subjected to a Superdex 200 Increase 10/300 GL column (GE Healthcare) pre-equilibrated with buffer containing 20 mM HEPES, pH 7.5, 100 mM NaCl, 2 mM $MgCl_2$, 100 μM TCEP, 10 μM GHRH, and 0.001% (wt/vol) digitonin (Anatrace). The monomeric fractions of the SV1–G_s complex were collected and concentrated to 10 to 20 mg/mL for cryo-EM examination.

Cryo-EM Data Collection and Image Processing. The freshly purified complexes (3.0 μL) at a final concentration of 17 mg/mL were applied to glow-discharged holey carbon grids (Quantifoil R1.2/1.3, 200 mesh) and subsequently vitrified using a Vitrobot Mark IV (Thermo Fisher Scientific). Cryo-EM images were collected on a Titan Krios microscope (FEI) equipped with a K3 Summit direct electron detector (Gatan, Inc.) in the Cryo-Electron Microscopy Research Center at Shanghai Institute of Materia Medica, Chinese Academy of Sciences. A total of 7,344 movies for the *apo* SV1–G_s complex were automatically acquired using SerialEM (66) in superresolution counting mode at a pixel size of 0.5225 Å and with defocus values ranging from −1.2 to −2.2 μm. Movies with 36 frames each were collected at a dose of 25 electrons per pixel per second over an exposure time of 3.2 s, resulting in an accumulated of dose of 73 electrons/$Å^2$ on sample. Image stacks of the *apo* SV1–G_s complex were aligned using MotionCor 2.1 (67). Contrast transfer function (CTF) parameters were estimated by Gctf v1.18 (68). The following data processing was performed using RELION-3.0-beta2 (69). Automated particle selection using Gaussian blob detection produced 4,949,167 particles from 7,344 micrographs. The particles were subjected to reference-free two-dimensional (2D) classification to discard fuzzy particles, resulting in 2,298,424 particles for further processing. The map of GHRH–GHRHR–G_s complex (18) (EMD-30505) low-pass filtered to 60 Å was used as the reference map for three-dimensional (3D) classification, generating one well-defined subset with 680,397 particles. Further 3D classifications focusing the alignment on the complex produced three good subsets accounting for 377,241 particles, which were subsequently subjected to 3D refinement, CTF refinement, and Bayesian polishing. The final refinement generated a map with an indicated global resolution of 2.6 Å at a Fourier shell correlation (FSC) of 0.143. For the GHRH–SV1–G_s complex, images were collected on a Titan Krios electron microscope (ThermoFisher Scientific) operating at 300 kV accelerating voltage at a calibrated magnification of 130,000× using a K2 Summit direct electron camera (Gatan) in counting mode with a Gatan Quantum energy filter. Movies were taken in energy-filtered transmission electron microscopy nanoprobe mode with a 50 μm C2 aperture corresponding to a magnified pixel size of 2.08 Å on the specimen level. In total, 2,397 movies were obtained with a defocus range of −1.2 to −2.2 μm. An accumulated dose of 80 electrons/$Å^2$ was fractionated into a movie stack of 36 frames. Dose-fractionated image stacks were subjected to beam-induced motion correction using MotionCor2.1 (67). A sum of all frames, filtered according to the exposure dose, in each image stack was used for further processing. CTF parameters for each micrograph were determined by Gctf v1.06 (68). Particle selection and 2D and 3D classifications were performed using RELION-3.0-beta2 (69). Auto-picking yielded 1,632,591 particle projections that were subjected to reference-free 2D classification to discard false-positive particles or particles categorized in poorly defined classes, producing 942,827 particle projections for further processing. This subset of particle projections was subjected to a round of maximum likelihood–based 3D classifications with a pixel size of 2.08 Å, resulting in one well-defined subset with 612,594 projections. Further 3D classifications with a mask on the complex produced one good subset accounting for 391,236 particles, which were subsequently subjected to a round of 3D classifications with a mask on the receptor. A selected subset containing 277,500 projections was then subjected to 3D refinement and Bayesian polishing with a pixel size of 1.04 Å. The final map has an indicated global resolution of 3.29 Å at an FSC of 0.143.

Model Building and Refinement. The final density maps of GHRH–SV1–G_s and *apo* SV1–G_s were automatically postprocessed using DeepEMhancer (70) to improve the electron microscopy (EM) map quality before model building. For both structures, the initial GHRH, SV1, and G_s heterotrimer models were taken from the GHRH–GHRHR–G_s–Nb35 complex (18) (Protein Data Bank [PDB] number: 7CZ5) and mini-G_s heterotrimer was taken from the GPR52–mini-G_s complex (71) (PDB number: 6LI3). All models were fitted into the EM density using University of California, San Francisco Chimera (72) followed by iterative manual adjustment in COOT (73) according to side-chain densities. The models were then subjected to ISOLDE (74) for further rebuilding and finalized using real-space refinement in PHENIX (75). The final model statistics for both structures were validated using "comprehensive validation (cryo-EM)" in PHENIX and are provided in the supplementary

information (*SI Appendix*, Table S3). All structural figures were prepared using Chimera (72), Chimera X (76), and PyMOL (https://pymol.org/2/).

cAMP Accumulation Assay. GHRH-stimulated cAMP accumulation was measured by a LANCE Ultra cAMP kit (PerkinElmer). Briefly, HEK293T cells (24 h after transfection with SV1 or GHRHR) or prostate cancer cells were digested by 0.2% (wt/vol) EDTA and washed once with Dulbecco's phosphate-buffered saline (PBS). Cells were then resuspended with stimulation buffer (Hanks' balanced salt solution [HBSS] supplemented with 5 mM HEPES, 0.5 mM IBMX, and 0.1% [wt/vol] bovine serum albumin [BSA], pH 7.4) to a density of 0.6 million cells per milliliter and added to 384-well white plates (3,000 cells per well). Different concentrations (5 μL) of GHRH were then added, and the stimulation lasted for 30 min at RT. The reaction was stopped by adding 5 μL Eu-cAMP tracer and 5 μL ULight-anti-cAMP. After 1 h RT incubation, TR-FRET signals (excitation: 320 nm, emission: 615 and 665 nm) were measured by an Envision plate reader (PerkinElmer). cAMP concentrations were interpolated by a standard curve.

G Protein NanoBiT Assay. HEK293T cells were seeded at a density of 30,000 cells per well into 96-well culture plates pretreated with poly-D-lysine hydrobromide. After incubation for 24 h to reach 70% to 80% confluence, the cells were transiently transfected with GHRHR or SV1, $Gα_s$-LgBiT, Gβ1, and Gγ2-SmBiT, at a 2:1:5:5 mass ratio. Twenty-four hours after transfection, cells were washed once and incubated for 30 min at 37 °C with HBSS buffer (pH 7.4) supplemented with 0.1% BSA and 10 mM HEPES. They were then reacted with coelenterazine H (5 μM) for 1 h at RT. Luminescence signals were measured using an Envision plate reader at 15-s intervals (25 °C). Briefly, following the baseline reading for 2.5 min, GHRH was added, and the reading continued for 25 min. Data were corrected to baseline and vehicle-treated samples. The area under the curve (AUC) across the time-course response curve was determined and normalized to the WT GHRHR, which was set to 100%.

β-arrestin 1/2 Recruitment Assay. HEK293T cells were seeded at a density of 30,000 cells per well into 96-well culture plates pretreated with poly-D-lysine hydrobromide. After incubation for 24 h to reach 70% to 80% confluence, the cells were transiently transfected with HA-Flag-GHRHR-Rluc8 or HA-Flag-SV1-Rluc8 and β-arrestin 1/2-Venus at a 1:9 mass ratio using lipofectamine 3000 reagent (Invitrogen) and cultured for another 24 h. Thereafter, cells were washed once and incubated for 30 min at 37 °C with HBSS buffer (pH 7.4) supplemented with 0.1% BSA and 10 mM HEPES. Five micro-molars of coelenterazine h (YEASEN Biotechnology) was then added and incubated for 5 min in the dark. The bioluminescence resonance energy transfer (BRET) signals were detected with an Envision plate reader by calculating the ratio of emission at 535 nm over emission at 470 nm. A 1.5-min baseline of BRET measurements was taken before the addition of GHRH and BRET signal was measured at 10-s intervals for further 9 min. After removing baseline and background readings by subtracting average values of the baseline measurement and average values of vehicle-treated samples, respectively, the AUC across the time-course response curve was determined and normalized to the WT GHRHR, which was set to 100%.

ERK1/2 Phosphorylation Assay. ERK1/2 phosphorylation was detected with the AlphaScreen SureFire ERK1/2 assay kit (PerkinElmer). Briefly, GHRHR or SV1 expressing HEK293T cells were seeded into 96-well culture plates coated with poly-D-lysine (30,000 cells/well) and grown overnight followed by deprivation of serum for at least 6 h. After incubation with FBS-free DMEM medium containing 4 μM GHRHR antagonist (MIA-602) or vehicle control for 30 min at RT, ERK1/2 phosphorylation was stimulated by the addition of 1 μM GHRH (100 μL final volume) at the indicated time points. GHRH stimulation was terminated by removal of medium and addition of 30 μL of SureFire lysis buffer to each well. The plate was then agitated for 15 min. A 1:17:100 (vol/vol/vol) dilution of AlphaScreen beads/SureFire activation buffer/SureFire reaction buffer was transferred to a white 384-well Proxiplate (8.5 μL per well) followed by addition of 5 μL lysate in diminished light. The plate was incubated in the dark at 37 °C for 1 h, after which the fluorescence signal was measured by an Envision plate reader using standard AlphaScreen settings. Data were normalized to the maximal response elicited by 10% FBS for 7 min followed by normalization to the maximal response elicited by GHRH.

Western Blot. To analyze phosphorylation of ERK, HEK293T cells (24 h after transfection with SV1 or GHRHR) or prostate cancer cells were stimulated by 1 μM GHRH at the indicated time points with or without pretreatment of 4 μM MIA-602. The cells were then lysed with radioimmunoprecipitation assay lysis buffer (Sigma-Aldrich) on ice for 5 min and centrifuged at 12,000 rpm for 15 min. Protein concentration of the supernatant was determined by BCA

protein assay kit (Beyotime). Proteins were loaded onto 10% sodium dodecyl sulfate-polyacrylamide gel with sodium dodecyl sulfate-loading buffer (Beyotime), separated by electrophoresis, and transferred to polyvinylidene difluoride membranes (0.2 μm; Merck Millipore). The membranes were blocked with 5% BSA in Tris-buffered saline Tween (TBST) buffer for 2 h at RT and incubated overnight at 4 °C with primary antibodies against ERK1/2 (1:1,000; 9102s, Cell Signaling Technology), pERK1/2 (1:1,000; 9101s, Cell Signaling Technology), β-tubulin (1:1,000; 2146s, Cell Signaling Technology), GHRHR (1:800; ab76263, Abcam), and flag (1:800; F3165, Sigma). After washing three times with TBST buffer, the membranes were incubated with secondary antibodies (1:10,000; Cell Signaling Technology) for 1 h at RT. Protein bands were visualized by ECL Plus (Bio-Rad). Densitometric analysis was then performed to determine the relative expression of target proteins normalized to β-tubulin or GAPDH. ERK1/2 phosphorylation was estimated as a ratio of pERK over total ERK.

Cell Cycle Analysis. Cells were added at density of 3×10^5/well to 12-well plates and treated with GHRH at indicated concentrations for 6 h. Following the treatment, the cells were digested by trypsin and collected by centrifugation. Cell pellets were washed with PBS and fixed with 70% (vol/vol) ethanol at 4 °C overnight. Cells were again collected by centrifugation and washed twice with PBS. They were then resuspended in PBS containing 0.2% Triton X-100, 50 μg/mL propidium iodide (PI), and 100 mg/mL RNase A and incubated for 30 min at 4 °C in the dark. After incubation, fluorescence intensity was measured with a NovoCyte flow cytometer (Acea Biosciences). Cells were gated for PI staining and cell accumulation in G_1, and S and G_2/M phases were calculated using the NovoExpress software.

Molecular Dynamics Simulation. Previous structural studies (77–79) have reported three β-arrestin 1–bound GPCR complex structures (PDB numbers: 6TKO, 6PWC, and 6UP7) but that of β-arrestin 2–bound has yet to be revealed. Thus, all three β-arrestin 1–bound structures were used to build models. The structure of GHRH–SV1–G_s complex and β-arrestin 1 models were aligned to the published β-arrestin 1–bound GPCR complex structures to construct GHRH/SV1/β-arrestin 1 complex models. The missing backbone and side chains were added. Similarly, the GHRH/GHRHR/β-arrestin 1 complex models were built using the cryo-EM structure of WT GHRHR (18) (PDB code: 7CZ5). To build a simulation system, we placed the complex model into a 1-palmitoyl-2-oleoyl-sn-glycero-3-phosphocholine lipid bilayer. The lipid-embedded complex model was solvated in a periodic boundary condition box (100 × 100 × 185 Å) filled with TI3P water molecules and 0.15 M KCl using CHARMM-GUI (80, 81). Each system was replicated to perform two independent simulations. On the basis of the CHARMM36m all-atom force field (82, 83), MD simulations were conducted using GROMACS 5.1.4 (84, 85). After 100-ns equilibration, the β-arrestin models built based on β-arrestin 1 binding to β1-adrenoreceptor (PDB number: 6TKO) produced stable conformations. Thus, a 1-μs production run was carried out for each simulation of these models. All productions were conducted in the isothermal–isobaric ensemble at temperature of 303.15 K and a pressure of 1 atm. Temperature and pressure were controlled using the velocity-rescale thermostat (86) and

the Parrinello-Rahman barostat with isotropic coupling (87), respectively. Equations of motion were integrated with a 2-fs time step, the LINCS algorithm was used to constrain bond length (88). Nonbonded pair lists were generated every 10 steps using a distance cutoff of 1.4 nm. A cutoff of 1.2 nm was used for Lennard-Jones (excluding scales 1 to 4) interactions, which were smoothly switched off between 1 and 1.2 nm. Electrostatic interactions were computed using a particle-mesh-Ewald algorithm with a real-space cutoff of 1.2 nm (89). The last 200-ns trajectory of each simulation was used to calculate average values. The distance between two residues is the minimal distance between nonhydrogen atoms from two different residues; the distance between the nonhydrogen atoms from the same residue was excluded. The backbone distance between two motifs is the minimal distance between backbone atoms from two different defined motifs; the distance between the backbone atoms from the same motif was excluded. The frequency of a particular residue interacting with a peptide was calculated by counting how many times this residue interacts with the peptide in the simulation snapshots. The interaction is defined by the nonhydrogen atom distance between the residue and the peptide using 4 Å as cutoff. The interacting frequency value indicates the stability of a particular residue–peptide interaction. A large interacting frequency indicates a stable interaction.

Statistical Analysis. All functional study data were analyzed using Prism 7 (GraphPad) and presented as means ± SEM from at least three independent experiments. Concentration-response curves were evaluated with a three-parameter logistic equation. The significance was determined with either two-tailed Student's t test or one-way ANOVA, and $P < 0.05$ is considered statistically significant.

1. N. J. Pavlos, P. A. Friedman, GPCR signaling and trafficking: The long and short of it. *Trends Endocrinol. Metab.* **28**, 213–226 (2017).
2. G. F. Marrone *et al.*, Truncated mu opioid GPCR variant involvement in opioid-dependent and opioid-independent pain modulatory systems within the CNS. *Proc. Natl. Acad. Sci. U.S.A.* **113**, 3663–3668 (2016).
3. R. Maggio *et al.*, Variants of G protein-coupled receptors: A reappraisal of their role in receptor regulation. *Biochem. Soc. Trans.* **44**, 589–594 (2016).
4. Y. A. Berchiche, T. P. Sakmar, CXC chemokine receptor 3 alternative splice variants selectively activate different signaling pathways. *Mol. Pharmacol.* **90**, 483–495 (2016).
5. S. Bailey *et al.*, Interactions between RAMP2 and CRF receptors: The effect of receptor subtypes, splice variants and cell context. *Biochim. Biophys. Acta Biomembr.* **1861**, 997–1003 (2019).
6. S. G. Furness, D. Wootten, A. Christopoulos, P. M. Sexton, Consequences of splice variation on Secretin family G protein-coupled receptor function. *Br. J. Pharmacol.* **166**, 98–109 (2012).
7. K. P. Minneman, Splice variants of G protein-coupled receptors. *Mol. Interv.* **1**, 108–116 (2001).
8. D. Markovic, R. A. Challiss, Alternative splicing of G protein-coupled receptors: Physiology and pathophysiology. *Cell. Mol. Life Sci.* **66**, 3337–3352 (2009).
9. P. Gris *et al.*, A novel alternatively spliced isoform of the mu-opioid receptor: Functional antagonism. *Mol. Pain* **6**, 1744–8069 (2010).
10. C. P. Nelson, R. A. Challiss, "Phenotypic" pharmacology: The influence of cellular environment on G protein-coupled receptor antagonist and inverse agonist pharmacology. *Biochem. Pharmacol.* **73**, 737–751 (2007).
11. A. Kahles *et al.*; Cancer Genome Atlas Research Network, Comprehensive analysis of alternative splicing across tumors from 8,705 patients. *Cancer Cell* **34**, 211–224.e6 (2018).
12. Z. Rekasi, T. Czompoly, A. V. Schally, G. Halmos, Isolation and sequencing of cDNAs for splice variants of growth hormone-releasing hormone receptors from human cancers. *Proc. Natl. Acad. Sci. U.S.A.* **97**, 10561–10566 (2000).
13. O. Moussa *et al.*, Novel role of thromboxane receptors beta isoform in bladder cancer pathogenesis. *Cancer Res.* **68**, 4097–4104 (2008).
14. M. R. Hellmich *et al.*, Human colorectal cancers express a constitutively active cholecystokinin-B/gastrin receptor that stimulates cell growth. *J. Biol. Chem.* **275**, 32122–32128 (2000).
15. M. U. Körner *et al.*, Wild-type and splice-variant secretin receptors in lung cancer: Overexpression in carcinoid tumors and peritumoral lung tissue. *Mod. Pathol.* **21**, 387–395 (2008).
16. J. E. Taylor, M. A. Theveniau, R. Bashirzadeh, T. Reisine, P. A. Eden, Detection of somatostatin receptor subtype 2 (SSTR2) in established tumors and tumor cell lines: Evidence for SSTR2 heterogeneity. *Peptides* **15**, 1229–1236 (1994).
17. X. Xiong *et al.*, Splice variant of growth hormone-releasing hormone receptor drives esophageal squamous cell carcinoma conferring a therapeutic target. *Proc. Natl. Acad. Sci. U.S.A.* **117**, 6726–6732 (2020).
18. F. Zhou *et al.*, Structural basis for activation of the growth hormone-releasing hormone receptor. *Nat. Commun.* **11**, 1–10 (2020).
19. K. E. Mayo, P. A. Godfrey, S. T. Suhr, D. J. Kulik, J. O. Rahal, Growth hormone-releasing hormone: Synthesis and signaling. *Recent Prog. Horm. Res.* **50**, 35–73 (1995).
20. R. Guillemin *et al.*, Growth hormone-releasing factor from a human pancreatic tumor that caused acromegaly. *Science* **218**, 585–587 (1982).

Cong et al.
Constitutive signal bias mediated by the human GHRHR splice variant 1

PNAS | 9 of 10
https://doi.org/10.1073/pnas.2106606118

21. J. Rivier, J. Spiess, M. Thorner, W. Vale, Characterization of a growth hormone-releasing factor from a human pancreatic islet tumour. *Nature* **300**, 276–278 (1982).
22. H. Kiaris, A. V. Schally, J. L. Varga, K. Groot, P. Armatis, Growth hormone-releasing hormone: An autocrine growth factor for small cell lung carcinoma. *Proc. Natl. Acad. Sci. U.S.A.* **96**, 14894–14898 (1999).
23. S. Buchholz *et al*., Potentiation of mammary cancer inhibition by combination of antagonists of growth hormone-releasing hormone with docetaxel. *Proc. Natl. Acad. Sci. U.S.A.* **104**, 1943–1946 (2007).
24. A. Klukovits *et al*., Novel antagonists of growth hormone-releasing hormone inhibit growth and vascularization of human experimental ovarian cancers. *Cancer* **118**, 670–680 (2012).
25. H. M. Wu *et al*., Growth hormone-releasing hormone antagonist inhibits the invasiveness of human endometrial cancer cells by down-regulating twist and N-cadherin expression. *Oncotarget* **8**, 4410–4421 (2017).
26. J. Gan *et al*., Growth hormone-releasing hormone receptor antagonists inhibit human gastric cancer through downregulation of PAK1-STAT3/NF-κB signaling. *Proc. Natl. Acad. Sci. U.S.A.* **113**, 14745–14750 (2016).
27. R. Busto *et al*., The expression of growth hormone-releasing hormone (GHRH) and splice variants of its receptor in human gastroenteropancreatic carcinomas. *Proc. Natl. Acad. Sci. U.S.A.* **99**, 11866–11871 (2002).
28. W. K. Chu *et al*., Antagonists of growth hormone-releasing hormone receptor induce apoptosis specifically in retinoblastoma cells. *Proc. Natl. Acad. Sci. U.S.A.* **113**, 14396–14401 (2016).
29. C. D. Fahrenholtz *et al*., Preclinical efficacy of growth hormone-releasing hormone antagonists for androgen-dependent and castration-resistant human prostate cancer. *Proc. Natl. Acad. Sci. U.S.A.* **111**, 1084–1089 (2014).
30. F. G. Rick *et al*., Antagonists of growth hormone-releasing hormone inhibit growth of androgen-independent prostate cancer through inactivation of ERK and Akt kinases. *Proc. Natl. Acad. Sci. U.S.A.* **109**, 1655–1660 (2012).
31. A. V. Schally, J. L. Varga, J. B. Engel, Antagonists of growth-hormone-releasing hormone: An emerging new therapy for cancer. *Nat. Clin. Pract. Endocrinol. Metab.* **4**, 33–43 (2008).
32. Z. Rekasi *et al*., Antiproliferative actions of growth hormone-releasing hormone antagonists on MiaPaCa-2 human pancreatic cancer cells involve cAMP independent pathways. *Peptides* **22**, 879–886 (2001).
33. H. Kiaris *et al*., Expression of a splice variant of the receptor for GHRH in 3T3 fibroblasts activates cell proliferation responses to GHRH analogs. *Proc. Natl. Acad. Sci. U.S.A.* **99**, 196–200 (2002).
34. M. Marti-Solano *et al*., Combinatorial expression of GPCR isoforms affects signalling and drug responses. *Nature* **587**, 650–656 (2020).
35. C. Christodoulou *et al*., Expression of growth hormone-releasing hormone (GHRH) and splice variant of GHRH receptors in normal mouse tissues. *Regul. Pept.* **136**, 105–108 (2006).
36. N. Barabutis *et al*., Stimulation of proliferation of MCF-7 breast cancer cells by a transfected splice variant of growth hormone-releasing hormone receptor. *Proc. Natl. Acad. Sci. U.S.A.* **104**, 5575–5579 (2007).
37. A. Havt *et al*., The expression of the pituitary growth hormone-releasing hormone receptor and its splice variants in normal and neoplastic human tissues. *Proc. Natl. Acad. Sci. U.S.A.* **102**, 17424–17429 (2005).
38. N. Dioufa *et al*., Growth hormone-releasing hormone receptor splice variant 1 is frequently expressed in oral squamous cell carcinomas. *Horm. Cancer* **3**, 172–180 (2012).
39. H. Kiaris *et al*., Ligand-dependent and -independent effects of splice variant 1 of growth hormone-releasing hormone receptor. *Proc. Natl. Acad. Sci. U.S.A.* **100**, 9512–9517 (2003).
40. N. Barabutis *et al*., Activation of mitogen-activated protein kinases by a splice variant of GHRH receptor. *J. Mol. Endocrinol.* **44**, 127–134 (2010).
41. K. Eichel, D. Jullié, M. von Zastrow, β-Arrestin drives MAP kinase signalling from clathrin-coated structures after GPCR dissociation. *Nat. Cell Biol.* **18**, 303–310 (2016).
42. T. Bourquard *et al*., Unraveling the molecular architecture of a G protein-coupled receptor/β-arrestin/Erk module complex. *Sci. Rep.* **5**, 1–13 (2015).
43. J. Duan *et al*., Cryo-EM structure of an activated VIP1 receptor-G protein complex revealed by a NanoBiT tethering strategy. *Nat. Commun.* **11**, 1–10 (2020).
44. D. Wootten, J. Simms, L. J. Miller, A. Christopoulos, P. M. Sexton, Polar transmembrane interactions drive formation of ligand-specific and signal pathway-biased family B G protein-coupled receptor conformations. *Proc. Natl. Acad. Sci. U.S.A.* **110**, 5211–5216 (2013).
45. G. Halmos *et al*., Expression of growth hormone-releasing hormone and its receptor splice variants in human prostate cancer. *J. Clin. Endocrinol. Metab.* **87**, 4707–4714 (2002).
46. I. Chatzistamou *et al*., Immunohistochemical detection of GHRH and its receptor splice variant 1 in primary human breast cancers. *Eur. J. Endocrinol.* **151**, 391–396 (2004).
47. I. Chatzistamou *et al*., Antagonists of growth hormone-releasing hormone and somatostatin analog RC-160 inhibit the growth of the OV-1063 human epithelial ovarian cancer cell line xenografted into nude mice. *J. Clin. Endocrinol. Metab.* **86**, 2144–2152 (2001).
48. H. Wang *et al*., Inhibition of experimental small-cell and non-small-cell lung cancers by novel antagonists of growth hormone-releasing hormone. *Int. J. Cancer* **142**, 2394–2404 (2018).
49. N. Dioufa *et al*., Growth hormone-releasing hormone receptor splice variant 1 is frequently expressed in oral squamous cell carcinomas. *Horm. Cancer* **3**, 172–180 (2012).
50. I. Chatzistamou, A. A. Volakaki, A. V. Schally, H. Kiaris, C. Kittas, Expression of growth hormone-releasing hormone receptor splice variant 1 in primary human melanomas. *Regul. Pept.* **147**, 33–36 (2008).
51. L. J. Clark *et al*., Allosteric interactions in the parathyroid hormone GPCR-arrestin complex formation. *Nat. Chem. Biol.* **16**, 1096–1104 (2020).
52. J. S. Smith, R. J. Lefkowitz, S. Rajagopal, Biased signalling: From simple switches to allosteric microprocessors. *Nat. Rev. Drug Discov.* **17**, 243–260 (2018).
53. M. A. Kjelsberg, S. Cotecchia, J. Ostrowski, M. G. Caron, R. J. Lefkowitz, Constitutive activation of the alpha 1B-adrenergic receptor by all amino acid substitutions at a single site. Evidence for a region which constrains receptor activation. *J. Biol. Chem.* **267**, 1430–1433 (1992).
54. E. Ceraudo *et al*., Direct evidence that the GPCR CysLTR2 mutant causative of uveal melanoma is constitutively active with highly biased signaling. *J. Biol. Chem.* **296**, 100163 (2021).
55. X. Chen, B. Bai, Y. Tian, H. Du, J. Chen, Identification of serine 348 on the apelin receptor as a novel regulatory phosphorylation site in apelin-13-induced G protein-independent biased signaling. *J. Biol. Chem.* **289**, 31173–31187 (2014).
56. L. Wanka *et al*., C-terminal motif of human neuropeptide Y4 receptor determines internalization and arrestin recruitment. *Cell. Signal.* **29**, 233–239 (2017).
57. W. Sun *et al*., A unique hormonal recognition feature of the human glucagon-like peptide-2 receptor. *Cell Res.* **30**, 1098–1108 (2020).
58. Y. L. Liang *et al*., Dominant negative G proteins enhance formation and purification of agonist-GPCR-G protein complexes for structure determination. *ACS Pharmacol. Transl. Sci.* **1**, 12–20 (2018).
59. F. Zhou *et al*., Molecular basis of ligand recognition and activation of human V2 vasopressin receptor. *Cell Res.* **31**, 929–931. (2021).
60. Z. Cong *et al*., Molecular insights into ago-allosteric modulation of the human glucagon-like peptide-1 receptor. *Nat. Commun.* **12**, 3763 (2021).
61. B. Carpenter, R. Nehmé, T. Warne, A. G. Leslie, C. G. Tate, Structure of the adenosine A(2A) receptor bound to an engineered G protein. *Nature* **536**, 104–107 (2016).
62. S. Maeda, Q. Qu, M. J. Robertson, G. Skiniotis, B. K. Kobilka, Structures of the M1 and M2 muscarinic acetylcholine receptor/G-protein complexes. *Science* **364**, 552–557 (2019).
63. S. Maeda *et al*., Development of an antibody fragment that stabilizes GPCR/G-protein complexes. *Nat. Commun.* **9**, 3712 (2018).
64. Y. Kang *et al*., Cryo-EM structure of human rhodopsin bound to an inhibitory G protein. *Nature* **558**, 553–558 (2018).
65. S. G. Rasmussen *et al*., Crystal structure of the β2 adrenergic receptor-Gs protein complex. *Nature* **477**, 549–555 (2011).
66. D. N. Mastronarde, Automated electron microscope tomography using robust prediction of specimen movements. *J. Struct. Biol.* **152**, 36–51 (2005).
67. S. Q. Zheng *et al*., MotionCor2: Anisotropic correction of beam-induced motion for improved cryo-electron microscopy. *Nat. Methods* **14**, 331–332 (2017).
68. K. Zhang, Gctf: Real-time CTF determination and correction. *J. Struct. Biol.* **193**, 1–12 (2016).
69. S. H. Scheres, RELION: Implementation of a Bayesian approach to cryo-EM structure determination. *J. Struct. Biol.* **180**, 519–530 (2012).
70. R. Sanchez-Garcia, J. Gomez-Blanco, A. Cuervo, J. M. Carazo, C. O. S. Sorzano, J. Vargas, DeepEMhancer: A deep learning solution for cryo-EM volume post-processing. *Commun. Biol.* **4**, 874 (2021).
71. X. Lin *et al*., Structural basis of ligand recognition and self-activation of orphan GPR52. *Nature* **579**, 152–157 (2020).
72. E. F. Pettersen *et al*., UCSF Chimera—A visualization system for exploratory research and analysis. *J. Comput. Chem.* **25**, 1605–1612 (2004).
73. P. Emsley, K. Cowtan, Coot: Model-building tools for molecular graphics. *Acta Crystallogr. D Biol. Crystallogr.* **60**, 2126–2132 (2004).
74. T. I. Croll, ISOLDE: A physically realistic environment for model building into low-resolution electron-density maps. *Acta Crystallogr. D Struct. Biol.* **74**, 519–530 (2018).
75. P. D. Adams *et al*., PHENIX: A comprehensive Python-based system for macromolecular structure solution. *Acta Crystallogr. D Biol. Crystallogr.* **66**, 213–221 (2010).
76. E. F. Pettersen *et al*., UCSF ChimeraX: Structure visualization for researchers, educators, and developers. *Protein Sci.* **30**, 70–82 (2021).
77. Y. Lee *et al*., Molecular basis of β-arrestin coupling to formoterol-bound β1-adrenoceptor. *Nature* **583**, 862–866 (2020).
78. W. Huang *et al*., Structure of the neurotensin receptor 1 in complex with β-arrestin 1. *Nature* **579**, 303–308 (2020).
79. W. Yin *et al*., A complex structure of arrestin-2 bound to a G protein-coupled receptor. *Cell Res.* **29**, 971–983 (2019).
80. E. L. Wu *et al*., CHARMM-GUI Membrane Builder toward realistic biological membrane simulations. *J. Comput. Chem.* **35**, 1997–2004 (2014).
81. S. Jo, T. Kim, V. G. Iyer, W. Im, CHARMM-GUI: A web-based graphical user interface for CHARMM. *J. Comput. Chem.* **29**, 1859–1865 (2008).
82. O. Guvench *et al*., CHARMM additive all-atom force field for carbohydrate derivatives and its utility in polysaccharide and carbohydrate-protein modeling. *J. Chem. Theory Comput.* **7**, 3162–3180 (2011).
83. A. D. MacKerell *et al*., All-atom empirical potential for molecular modeling and dynamics studies of proteins. *J. Phys. Chem. B* **102**, 3586–3616 (1998).
84. D. Van Der Spoel *et al*., GROMACS: Fast, flexible, and free. *J. Comput. Chem.* **26**, 1701–1718 (2005).
85. B. Hess, C. Kutzner, D. van der Spoel, E. Lindahl, GROMACS 4: Algorithms for highly efficient, load-balanced, and scalable molecular simulation. *J. Chem. Theory Comput.* **4**, 435–447 (2008).
86. G. Bussi, D. Donadio, M. Parrinello, Canonical sampling through velocity rescaling. *J. Chem. Phys.* **126**, 014101 (2007).
87. K. M. Aoki, F. Yonezawa, Constant-pressure molecular-dynamics simulations of the crystal-smectic transition in systems of soft parallel spherocylinders. *Phys. Rev. A* **46**, 6541–6549 (1992).
88. B. Hess, P-LINCS: A parallel linear constraint solver for molecular simulation. *J. Chem. Theory Comput.* **4**, 116–122 (2008).
89. T. Darden, D. York, L. Pedersen, Particle mesh Ewald - An N.Log(N) method for Ewald sums in large systems. *J. Chem. Phys.* **98**, 10089–10092 (1993).